

Dipole Moment and Charge Reorganization in Photoredox Catalysts

Justin Earley

University of Colorado Boulder

Anna Zieleniewska

National Renewable Energy Lab

Hunter Ripberger

Princeton University

Megan Lazorski

National Renewable Energy Lab

Zachary Mast

National Renewable Energy Lab

Hannah Sayre

Princeton University

Robert Knowles

Princeton University <https://orcid.org/0000-0003-1044-4900>

James McCusker

Michigan State University <https://orcid.org/0000-0002-5684-3117>

Gregory Scholes

Princeton University <https://orcid.org/0000-0003-3336-7960>

Obadiah Reid

University of Colorado Boulder <https://orcid.org/0000-0003-0646-3981>

Garry Rumbles (✉ garry.rumbles@nrel.gov)

National Renewable Energy Laboratory

Article

Keywords: Ion Pair Reorganisation, Microwave-frequency Dielectric-loss Measurements, Dipolar Relaxation Time, Catalytic Activity

Posted Date: July 6th, 2021

DOI: <https://doi.org/10.21203/rs.3.rs-639483/v1>

License: © ⓘ This work is licensed under a Creative Commons Attribution 4.0 International License.

[Read Full License](#)

Version of Record: A version of this preprint was published at Nature Chemistry on April 14th, 2022. See the published version at <https://doi.org/10.1038/s41557-022-00911-6>.

Dipole Moment and Charge Reorganization in Photoredox Catalysts

J.D. Earley^{1, 2+}, A. Zieleniewska¹⁺, H.H. Ripberger³, M.S. Lazorski^{1,4}, Z.J. Mast¹, H. Sayre³, R.R. Knowles³, J.K. McCusker⁵, G.D. Scholes³, O.G. Reid^{1, 6}, and G. Rumbles^{1,2,6}

¹National Renewable Energy Lab, Golden, 80401, USA

²University of Colorado Boulder, Department of Chemistry, Boulder, 80309, USA

³Princeton University, Department of Chemistry, Princeton, 08544, USA

⁴Metropolitan State University of Denver, Department of Chemistry and Biochemistry, Denver, 80204, USA

⁵Michigan State University, Department of Chemistry, Ann Arbor, 48824, USA

⁶University of Colorado Boulder, Renewable and Sustainable Energy Institute, Boulder, 80309, USA

*Garry.Rumbles@nrel.gov

+these authors contributed equally to this work

ABSTRACT

We report evidence of excited-state ion pair reorganisation in a cationic iridium (III) photoredox catalyst in 1,4-dioxane. Microwave-frequency dielectric-loss measurements combined with accurate calculations of dipolar relaxation time allow us to assign both ground and excited-state molecular dipole moments in solution and determine the polarizability volume in the excited-state. These measurements show significant changes in ground-state dipole moment between $[Ir[dF(CF_3)ppy]_2(dtbbpy)]PF_6$ (10.74 Debye) and $[Ir[dF(CF_3)ppy]_2(dtbbpy)]BAR_4^F$ (4.86 Debye). Photoexcitation of each complex results in population of highly mixed ligand centered and metal-to-ligand charge transfer states with enormous polarizability. Relaxation to the lowest lying excited-state leads to a negative change in the dipole moment for $[Ir[dF(CF_3)ppy]_2(dtbbpy)]PF_6$, and a positive change in dipole moment for $[Ir[dF(CF_3)ppy]_2(dtbbpy)]BAR_4^F$. These observations are consistent with a sub-nanosecond reorganization with the PF_6^- counter-ion, which cancels the dipole moment of the lowest lying excited-state, a process which is absent for the BAR_4^F- counter-ion. Taken together, these observations suggest contact-ion pair formation between the cationic metal complex and the PF_6^- anion and, at most, solvent-separated pairing with BAR_4^F- . The dynamic ion pair reorganisation we observe with the PF_6^- counter-ion may substantially modify both the thermodynamic potential available for electron transfer and kinetically inhibit oxidative catalysis, as the anion moves to cover the positively charged end of the molecule, providing a possible mechanistic explanation for recently observed trends in the catalytic activity of these complexes as a function of anion identity in low-polarity solvents. These tunable ion-pair dynamics could prove to be a valuable tool for tailoring the reactivity of both new and extant photocatalysts.

Introduction

Photoredox catalysts are able to drive reactions with high kinetic or thermodynamic barriers by harnessing the energy of light. This in-situ preparation of highly oxidizing or reducing reagents from stable precursors allows gentler more selective reaction conditions, opening the doors to many new reactions such as the processing of lignin into stock chemical species to aryl-dehalogenation reactions.¹⁻⁸

Cyclometalated (C[^]N) and polypyridyl (N[^]N) complexes of d_6 metals are some of the most promising transition metal photoredox catalysts to date. Heteroleptic compounds incorporating (C[^]N) and (N[^]N) ligands, as in $[Ir(ppy)_2(bpy)]^+$ complexes, benefit from independent tunability of HOMO and LUMO levels via ligand architecture.⁹⁻²⁰ Yet, the relationship between structural/environmental perturbations and changes in the intricate excited-state manifold of $[Ir(ppy)_2(bpy)]^+$ complexes are hard to capture with existing spectroscopies, making it commensurately difficult to understand all the factors that modulate their photoredox activity. Tuning of the redox potentials, absorption energy, excited-state lifetime, and quantum yield, are well known criteria, but other factors can play an important role.²¹⁻²⁴ For instance, recent work suggests that the size and polarity of the counter-ion effects the efficiency of the catalytic cycle,²⁵⁻³¹. While many reports note spectral changes due to ion-pairing in common photoredox catalysts,^{30,32-36} there are currently no direct quantitative methods that can probe the ground and excited-state electron density distribution to understand how ion pairing influences the excited state structure and evolution. Here, we introduce a modern implementation of time-resolved dielectric-loss spectroscopy (TRDL) to investigate how counter-ion identity influences the excited-state charge distribution within an important photoredox catalyst, $[Ir[dF(CF_3)ppy]_2(dtbbpy)]X$.³⁷⁻³⁹ We find large differences in both the ground and excited-state dipole moments depending on

33 whether X is a small associating anion (PF_6^-) that forms a contact-ion pair vs. a large one that either dissociates or forms a
34 solvent-separated pair (BAr_4^{F-}). These results suggest that ion pairing and the control it confers over both ground-state and
35 excited-state structure could be a heretofore underappreciated factor that modulates reactivity in ionic photoredox catalysts.

36 In what follows, we describe our modern implementation of TRDL using quantitative methods to measure complex
37 permittivity, and calculations of the dipole moment of both ground and excited-state molecules in solution. We use elec-
38 tromagnetic simulations to relate measured microwave resonator properties to the complex permittivity of the sample.
39 Combined with new quantitative calculations of the dipolar relaxation time, we are able to extract the molecular dipole
40 moment from dielectric-loss data. We verify the validity of our methods by studying the ground and excited-state dipole
41 moments of N,N-dimethylaminobenzonitrile (DMABN) in 1,4-dioxane; a model compound with a well understood *in*-
42 tramolecular charge transfer excited-state. Finally, we apply this approach to understand the excited-state charge reorganization
43 in $[Ir[dF(CF_3)ppy]_2(dtbpv)]PF_6$ and $[Ir[dF(CF_3)ppy]_2(dtbpv)]BAr_4^F$.

44 Dielectric-loss Spectroscopy Background

45 Flash-photolysis time-resolved dielectric-loss (fp-TRDL) spectroscopy is a perturbative technique developed to measure
46 the time dependent evolution of a molecule's electron density distribution; it is one of only a few methods to measure a
47 solution-phase molecule's excited-state dipole moment *in situ* without relying on emission, which can bias observations to
48 bright states and limit the broad applicability of the technique, for instance with dark molecular triplet states.^{40–43} In this
49 technique, microwave radiation is used to measure the complex permittivity ($\epsilon_r = \epsilon' - i\epsilon''$) of a sample by monitoring the
50 phase and amplitude changes of a transmitted waveform. Performing this measurement inside a resonance cavity increases the
51 effective path length through the sample and thus improves the sensitivity to small changes in ϵ_r . At the X-band frequencies
52 used in these experiments (8.2 - 12.4 GHz), changes in ϵ_r from a solution are a function of solute concentration, a solute's
53 dipole moment (μ), and its polarizability volume (V_p). Selectively exciting a photoredox catalyst with a pulsed laser allows
54 measurement of $\Delta\epsilon_r$ due to the solute molecule's change in dipole moment and polarizability volume – the change in charge
55 density and localization from the ground-state to the excited-state. Ultimately, measuring both ϵ_r and $\Delta\epsilon_r$ captures the dipole
56 moment and polarizability volume of a solution-phase sample, both in the ground and excited-states.

57 Our implementation of dielectric-loss spectroscopy consists of placing a sample inside a resonant microwave cavity and
58 measuring the change in cavity characteristics caused either as a function of ground or excited-state solute concentration.
59 Electromagnetic modeling is then used to relate the complex permittivity of the sample to the resonator properties, allowing
60 quantitative permittivity measurements. The modeling is combined with quantitative simulation of the dipolar relaxation time
61 to extract the molecular dipole moment and polarizability volume of the solute. [SI section *COMSOL Simulation of Microwave*
62 *Cavities*]

63 For this study, a new microwave resonance cavity (figure 1) was designed and fabricated to measure solution-phase samples
64 based on a design by Fessenden et. al.⁴⁴ The experimental set-up consists of a 5 mm diameter EPR tube placed in the cavity
65 at one electric field maximum of the TE_{102} standing wave, and a single slit in the end wall allowing for photoexcitation. A
66 circular iris structure is placed between the feeding waveguide and the cavity in order to couple microwave radiation into the
67 cavity, and define one end of the resonator. For all samples in this work, a 9.20 mm diameter iris was used unless otherwise
68 stated. Maxwell's equations were solved using the computer aided drafting (CAD) model and radio-frequency (RF) simulation
69 package COMSOL Multiphysics (v4.3a). This allowed us to optimize the sample position and iris diameter before fabricating
70 the microwave cavity; this design process has been described in our previous work.⁴⁵

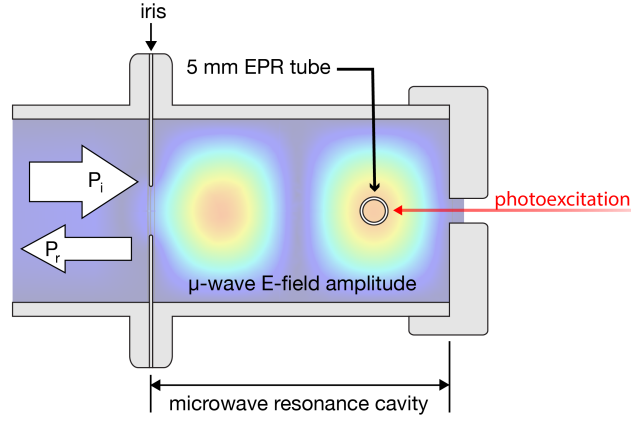


Figure 1. COMSOL Multiphysics electric-field amplitude solution for our solution-phase microwave resonance cavity.

71 After manufacturing the cavity, the reverse process was used to model the manufactured cavity in COMSOL to account for
 72 manufacturing defects, and extract quantitative values for the sensitivity of the cavity characteristics to the complex permittivity
 73 of the sample (ϵ' and ϵ''). [described in section *COMSOL Simulation of Microwave Cavities* of the SI] By iteratively stepping
 74 the simulated sample's ϵ' and ϵ'' inside the EPR tube, we create a look-up table of simulation results that we then use as a
 75 numerical fit function to quantify the dielectric properties of solution-phase samples; this enables us to convert measured
 76 microwave power reflectance as a function of frequency about the cavity resonance to ϵ' and ϵ'' .

77 The complex permittivity of a solution-phase sample is a function of both the dipole moment and polarizability of all the
 78 molecules therein, and for dilute solutions, it may be expressed as the sum of contributions from the solvent and the solute.
 79 This relationship is simplified if the complex permittivity can be separated into its real and imaginary components (described by
 80 equation (1)) as the imaginary permittivity is only a function of the dipole moment.

$$\epsilon_r = [\epsilon' - i\epsilon'']_{solute} + [\epsilon' - i\epsilon'']_{solvent} \quad (1)$$

81 The remainder of this discussion will focus only on the solute's contribution to the permittivity as the solvent's contribution is
 82 subtracted out in the experimental procedure.

83 Firstly, the real part of the solute's permittivity can be separated into two components which describe the dipole contribution
 84 (ϵ'_D) and the electronic polarizability contribution (ϵ'_E).

$$\epsilon' = \epsilon'_D + \epsilon'_E \quad (2)$$

85 Both components are derived from Debye's polarity equations of a polar molecule rotating in an electric field.⁴⁶ The dipole
 86 contribution to the real permittivity is described as:

$$\epsilon'_D = \frac{(\epsilon(0) + 2)(\epsilon(\infty) + 2)}{27\epsilon_0 k_B T} \frac{\mu^2}{(\omega\theta)^2} N f(\omega\theta) \quad (3)$$

87 Where N is the solute concentration in *molecules/m³*, ϵ_0 is the permittivity of free space, $\epsilon(0)$ is the DC dielectric constant
 88 of the solvent, $\epsilon(\infty)$ is the high-frequency dielectric constant of the solvent (which can be approximated as the square-root
 89 of the refractive index, \sqrt{n}), ω is the microwave angular frequency, μ is the molecule's dipole moment, k_B is the Boltzmann
 90 constant, θ is the dipolar relaxation time of the solute [described further in the *Molecular Rotation* section of the SI], and
 91 T is temperature. The function $f(\omega\theta)$ describes the variation in experimental sensitivity due to the correlation between the
 92 microwave frequency and the frequency of the dipole's relaxation.

$$f(\omega\theta) = \frac{(\omega\theta)^2}{1 + (\omega\theta)^2} \quad (4)$$

93 The electronic component of the real permittivity is a function of the solute's electronic polarizability (α_e).

$$\varepsilon'_E = \frac{(\varepsilon(0) + 2)(\varepsilon(\infty) + 2)}{9\varepsilon_0} \alpha_e N \quad (5)$$

94 In contrast to the real part, the imaginary part of the complex permittivity is only a function of the dipole moment and looks
95 similar to equation (3), however, the denominator term ($\omega\theta$) is not squared.

$$\varepsilon'' = \frac{(\varepsilon(0) + 2)(\varepsilon(\infty) + 2)}{27\varepsilon_0 k_B T} \frac{\mu^2}{\omega\theta} N f(\omega\theta) \quad (6)$$

96 **Ground-state dielectric-loss**

97 We calculate the ground-state dipole moment of a solute molecule by performing a series of measurements of ε'' as a
98 function of solute concentration. Rewriting equation (6) to reflect this experiment yields the following equation:

$$\Delta\varepsilon'' = \frac{(\varepsilon(0) + 2)(\varepsilon(\infty) + 2)}{27\varepsilon_0 k_B T} \frac{\mu_{GS}^2}{\omega\theta} \Delta N f(\omega\theta) \quad (7)$$

99 Where now the solute concentration changes (ΔN) thus changing $\Delta\varepsilon''$ and the solvent's contribution subtracts out. Dividing
100 both sides by ΔN in equation (7), provides an expression for the slope of this concentration-dependent study.

$$slope = \frac{\Delta\varepsilon''}{\Delta N} = \frac{(\varepsilon(0) + 2)(\varepsilon(\infty) + 2)}{27\varepsilon_0 k_B T} \frac{\mu_{GS}^2}{\omega\theta} f(\omega\theta) \quad (8)$$

101 Rearranging equation (8) gives the expression for the ground-state dipole moment.

$$\mu_{GS} = \sqrt{\frac{27\varepsilon_0 k_B T}{(\varepsilon(0) + 2)(\varepsilon(\infty) + 2)} \frac{\omega\theta}{f(\omega\theta)} \left[\frac{\Delta\varepsilon''}{\Delta N} \right]} \quad (9)$$

102 Once the slope of the $\Delta\varepsilon''$ vs. concentration has been measured, the only remaining unknown in this equation is the dipolar
103 rotational relaxation of the solute. We have implemented a numerical simulation package in Python which provides accurate
104 values for the dipolar rotational relaxation time using the molecular structure, solvent viscosity, solvent dielectric, and
105 temperature as input parameters [described further in the *Molecular Rotation* section of the SI] enabling accurate dipole moment
106 measurements without the need for carefully selected standards or outside experiments as was the case in the past.^{41,44} Due to
107 experimental sensitivity constants, we are unable to use this same technique in order to measure the ground-state polarizability
108 with much accuracy without going to unacceptably high solute concentrations.

109 **Excited-state transient dielectric-loss**

110 Photoexcitation is used to excite the sample and study the dipole moment and polarizability of the excited-states. In this
111 case, equation 3 describing the dipole component of the real permittivity becomes:

$$\Delta\varepsilon'_D(t) = \frac{(\varepsilon(0) + 2)(\varepsilon(\infty) + 2)}{27\varepsilon_0 k_B T} \frac{\mu_*^2 - \mu_{GS}^2}{(\omega\theta)^2} N_*(t) f(\omega\theta) \quad (10)$$

112 Where $N_*(t)$ is the excited-state solute concentration in *molecules/m³* as a function of time due to the sample's excited-state
113 kinetics, and μ_*^2 is the excited-state dipole moment. Equation (5) which describes the polarizability component of the real
114 permittivity becomes:

$$\Delta\varepsilon'_E(t) = \frac{(\varepsilon(0) + 2)(\varepsilon(\infty) + 2)}{9\varepsilon_0} \Delta\alpha_e N_*(t) \quad (11)$$

115 Change in electronic polarizability is related to the polarizability volume (ΔV_p) which qualitatively describes the localization
116 volume of a molecular excited-state.⁴⁷

$$\Delta V_p = \frac{\Delta\alpha_e}{4\pi\epsilon_0} \quad (12)$$

117 Finally, the imaginary component of the complex permittivity becomes the following equation.

$$\Delta\epsilon''(t) = \frac{(\epsilon(0) + 2)(\epsilon(\infty) + 2)}{27\epsilon_0 k_B T} \frac{\mu_*^2 - \mu_{GS}^2}{\omega\theta} N_*(t) f(\omega\theta) \quad (13)$$

118 For transient measurements, we fit a global kinetic model to our data (detailed in the *Fitting TRDL Transients* section of the SI)
119 in order to get an excited-state concentration ($N_*(t)$) for each kinetic component. Then, the $\Delta\epsilon'$ and $\Delta\epsilon''$ values that relate to
120 those respective components are used to calculate the various changes in dipole moment and molecular polarizability volume.
121 The absolute value of the excited-state dipole moment can then be calculated knowing the ground-state dipole moment.

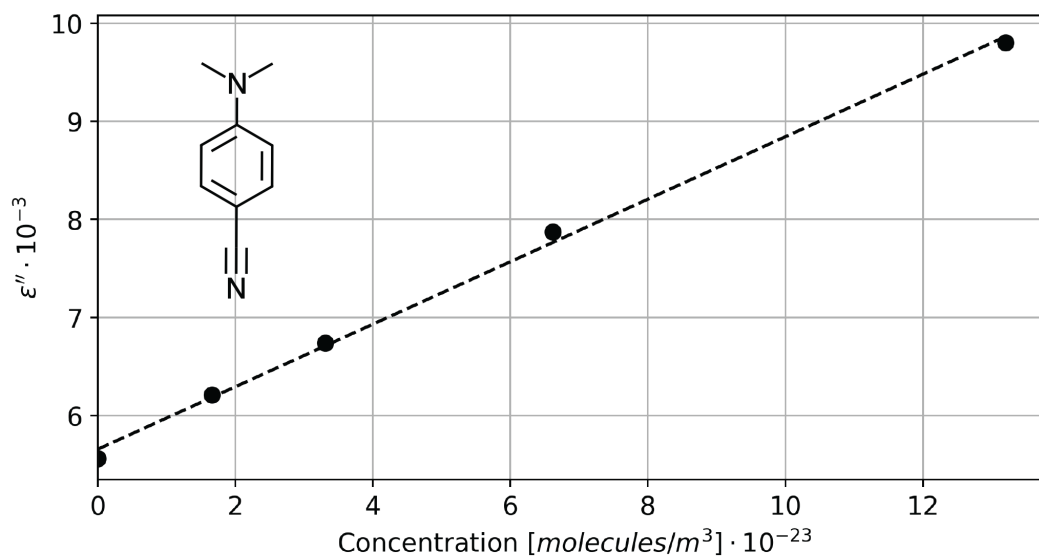
122 Thermal artifacts are easily measured in dielectric-loss spectroscopy due to its high sensitivity. These arise from transient
123 changes in the dielectric properties of the *solvent* as a function of local temperature. Since the TRDL signal is proportional to
124 the concentration of the excited species, small thermal changes in the *solvent* easily overwhelm larger changes in the *solute*
125 properties. To minimize this, TRDL must be performed in low dielectric-constant solvents so that thermally-induced changes
126 in its dielectric constant also remain small. For all of the work in this paper, 1,4-dioxane has been used as it has shown no
127 evidence of thermal artifacts in TRDL transients.

128 Validating our methods using N,N-dimethylaminobenzonitrile

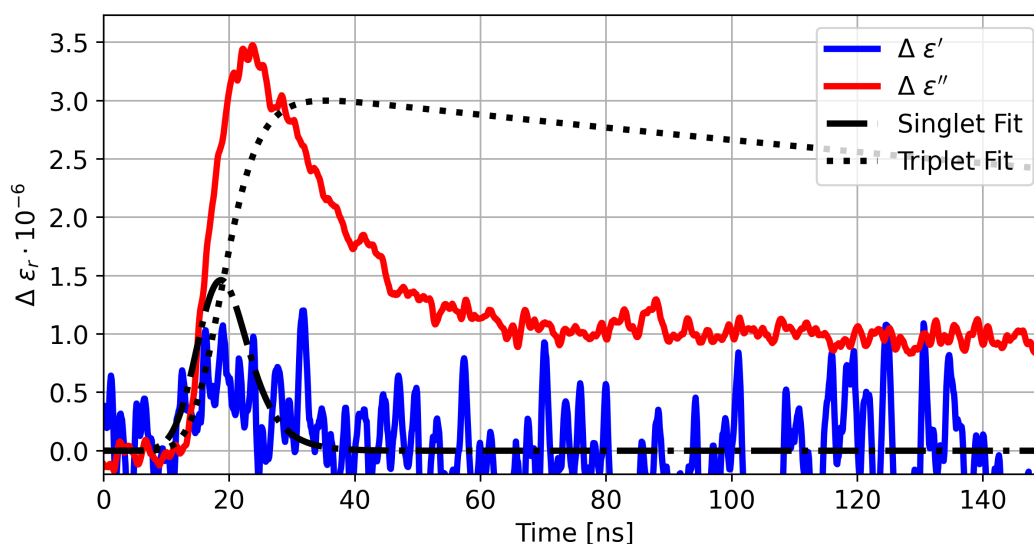
129 A donor-acceptor molecule, N,N-dimethylaminobenzonitrile, was used to test the validity of our COMSOL simulations,
130 dipolar relaxation time calculations, and overall analysis. DMABN has been extensively studied because of its intramolecular
131 charge-transfer (ICT) excited-state and resulting dual-emission; in particular, John Warman has reported on its kinetics,
132 ground-state dipole moment and excited-state dipole moments using dielectric-loss spectroscopy, making it an ideal reference
133 compound for our work.⁴⁸⁻⁵¹

134 DMABN has two singlet states in equilibrium, a locally excited-state (LE) and the intramolecular charge transfer state
135 (ICT). The LE state has a dipole moment that is only slightly larger than that in the ground-state at 9.7 D; whereas, the ICT
136 state's dipole moment is significantly larger than the ground-state at 15.1 D.⁵² The initial LE-ICT singlet state relaxes through a
137 triplet state that has a dipole moment approximately equal to that of the LE state, with its inter-system crossing yield being
138 correlated to the solvent's polarity. The CT state is stabilized by the solvent's polarity as well, thus the ratio of CT:LE is higher
139 in polar solvents and the CT state's dipole moment dominates the TRDL signal at early times when the singlet state is evolving.

140 Figure 2(a) shows a plot of imaginary permittivity as a function of DMABN concentration in 1,4-dioxane. Using the slope
141 of the linear fit, equation (9), and a θ of 33.4 ps, we found the ground-state dipole moment of DMABN to be 6.2 D. This is in
142 close agreement with the ground-state value for DMABN reported by Warman using TRDL: 6.6 D. This result demonstrates
143 the accuracy and precision with which we can measure the ground-state dipole moment of a molecule in solution using our
144 instrument and data analysis methods, and validates the calculations used to determine θ (described in the *Molecular Rotation*
145 section of the SI).



(a)



(b)

Figure 2. (a) Ground-state measurement of the imaginary permittivity as a function of DMABN concentration in 1,4-dioxane with the structure of DMABN as the inset. A linear fit of the form $y = 8.249 \cdot 10^{-27}x + 4.05 \cdot 10^{-3}$ is used to extract the change in permittivity per DMABN molecule, and extract a ground-state dipole moment of 6.2 D using equation (9). (b) complex permittivity transients for DMABN (red and blue) and the kinetic fitting results (black), showing the singlet and triplet species trajectories. The global fit lines to the real and imaginary transients are omitted for clarity. 300 nm excitation at $5.45 \cdot 10^{15} \text{ cm}^{-2}$, 7 ns FWHM pulse, [DMABN] = 0.15 mM in dioxane

146 Figure 2(b) shows the transient kinetics for 0.15 mM DMABN in 1,4-dioxane upon photoexcitation at 300 nm. Here, the
 147 real (blue) and imaginary (red) components of the of the transient change in permittivity are separated using the procedure
 148 described in the *Fitting COMSOL Models to Data and the Complex K-Factor* section of our SI, giving quantitative values for
 149 $\Delta\epsilon_r$. Notably, the noise level here is ~ 100 ppb in ϵ_r after averaging fewer than 100 laser shots (limited by the photostability of
 150 DMABN). The transient kinetics observed are similar to that reported by Warman when taking into account the differences
 151 in instrument response. Indeed, the kinetics are fit using an identical model to that employed by Warman, with certain key
 152 parameters fixed from his prior work: sequential conversion of the LE+ICT singlet to the triplet state in competition with

ground-state recovery.⁵² The black traces in Figure 2(b) show the kinetic trajectories assigned to the singlet (solid) and triplet (dashed) states. The conversion between the singlet and triplet states takes place too fast ($\sim 10^{10} \text{s}^{-1}$) for a TRDL experiment to properly constrain the kinetic fit, and we use TRPL results from the literature to fix this timescale in our model.⁵²⁻⁵⁴ Likewise, the TRDL experiment does not directly observe conversion of the singlet LE and ICT states to the ground-state in competition with intersystem crossing, and we fix the triplet yield based on prior results as well.⁵⁴ Thus, the only free fit parameters in our global kinetic model (over real and imaginary signals) is the triplet state lifetime and the change in ϵ_r per molecule. The rate constants associated with each state are summarized in (see Supplementary Table S3), and the extracted values for the transient dipole moments for the ground, singlet, and triplet excited-states are summarized in table 1. In agreement with the previous literature: (1) the singlet state of DMABN is dominated by the large dipole moment associated with the ICT state in 1,4-dioxane, and (2) the obtained triplet state dipole is substantially less than that of the singlet state.

Table 1. Dipole measurement literature comparison of DMABN in 1,4-dioxane.^{52,54}

	Experiment	Literature	Agreement
μ_{GS}	$6.2 \pm 0.2 \text{ D}$	6.6 D	94.1 %
$\Delta\mu_S$	$6.1 \pm 0.2 \text{ D}$	8.5 D	72.0 %
$\Delta\mu_T$	$1.78 \pm 0.05 \text{ D}$	3.1 D	57.5 %

The relatively weaker agreement (relative to literature) in the absolute excited-state dipole moments we calculate compared to the ground-state most likely arises from the difficulty in ascertaining the excited-state concentration, both in our case and in past measurements. Since the calculation of the transient dipole moment is coupled to the excited-state solute concentration, the accuracy of estimating this concentration introduces error into the resultant dipole value in cases such as this where much of the dynamics are instrument-response limited. Warman et. al. relied on internal actinometry for estimating the excited-state concentration and parallel TRPL measurements to fix kinetic parameters that were not measurable via TRDL. We use careful calibration of light absorption in our EPR-tube sample configuration and excited-state density simulations that account for saturable absorption effects [discussed in section *Excitation Density Calculations* in the SI]. Additionally, we observed sample degradation from laser excitation, which was minimized but possibly not eliminated, by handling all samples in a nitrogen glove box, limiting our analysis to averaging the first 100 transients, and refreshing sample intermittently throughout the measurement. The good agreement we obtain for the singlet state shows that these methods are effective, but the rather large discrepancy for the triplet dipole moment measurement suggests that the triplet yield may be substantially lower in our hands than the value found previously, which is fixed in our kinetic model at the literature value.⁵⁴

176 Contact-ion Pairing and Transient Dipole Moments in $[\text{Ir}[\text{dF}(\text{CF}_3)\text{ppy}]_2(\text{dtbpy})]\text{X}$

177 Having established the accuracy of our experimental methods via the well-studied ICT excited-state of DMABN, we turn
 178 to the more complex topic of the cationic photoredox catalysts $[\text{Ir}[\text{dF}(\text{CF}_3)\text{ppy}]_2(\text{dtbpy})]\text{X}$ (abbreviated: $\text{Ir}[\text{tBu}]\text{-X}$). Here,
 179 we expect a metal-to-ligand charge transfer (MLCT) state that is analogous to the ICT state of DMABN, but the presence of
 180 multiple ligands, large-spin-orbit coupling due to Ir(III) ($\xi_{c,\text{Ir}} = 3909 \text{cm}^{-1}$ vs. $\xi_{c,\text{soc,Ru(II)}} = 990 \text{cm}^{-1}$)⁵⁵, and ion pairing in a
 181 low dielectric constant solvent introduce new and unexpected dynamics. Below, we show that the highly mixed excited-states
 182 of our energetically similar ligands manifests as charge transfer processes from $\text{dF}(\text{CF}_3)\text{ppy}$ to dtbpy on the ns timescale.
 183 Meanwhile, contact-ion pairing introduces an *intermolecular* dipole moment between the two ionic species that dramatically
 184 changes the dipole of the excited-state through additional nuclear reorganization. These latter two effects vanish for a more
 185 weakly bound anion, whilst a flip-flopping inter-ligand charge transfer behavior at early times is consistent in both.

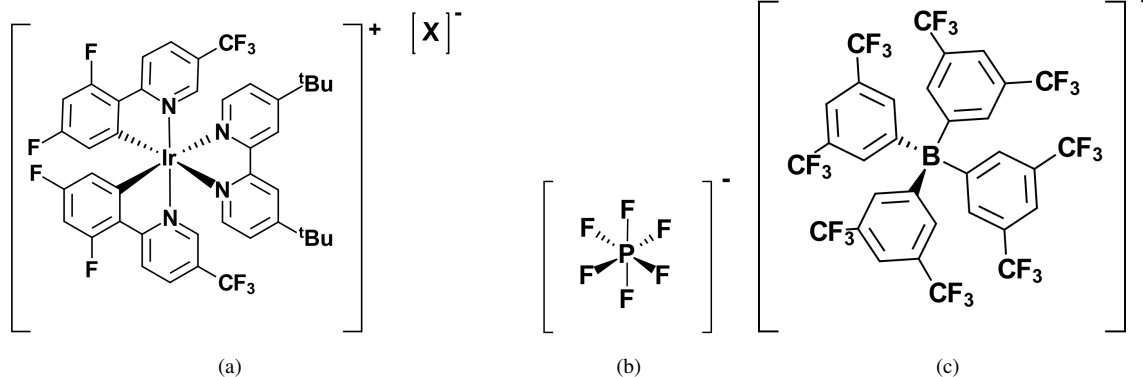


Figure 3. Structures of the iridium cation (a) $[Ir[dF(CF_3)ppy]_2(dt bpy)]X$ with anion X being (b) $X = PF_6^-$ (c) $X = BAr_4^{F-}$

186 Ion Pairing in the ground-state

187 We control ion pairing in $Ir[tBu]-X$ in 1,4-dioxane by tuning the size of the anion (X^-). Using PF_6^- as the counter ion
 188 is expected to result in contact-ion pairing in 1,4-dioxane due to its small size in relation to $[Ir[dF(CF_3)ppy]_2(dt bpy)]^+$
 189 (abbreviated: $Ir[tBu]^+$), whereas using the much bulkier *tetrakis[3,5-bis(trifluoromethyl)phenyl]borate*¹⁻ (BAr_4^{F-}) should shift
 190 the dissociation equilibrium so that contact-ion pairs no longer form, as $Ir[tBu]^+$ and BAr_4^{F-} are relatively the same size. As
 191 with DMABN, measuring the characteristics of the microwave cavity as a function of the $Ir[tBu]-X$ concentrations allows
 192 us to obtain their ground-state dipole moments. However, an additional complexity in this context is that it is necessary to
 193 make an assumption about whether contact-ion pairing takes place in order to calculate the rotational relaxation time of the
 194 complex, which can change significantly when the ion pair rotates as a unit. The approach we take here is to test each possibility
 195 (contact-paired vs. not) and observe whether the dipole moment we calculate is consistent with basic chemical theory and
 196 literature calculations.^{56–58} This provides an excellent method for assessing ion pairing in the ground-state of these complexes.
 197 The results of these elementary calculations are displayed in table 2.

Table 2. Predicted ground-state dipole moment between the iridium metal center and the anion's center using basic chemical theory ($\mu = d \cdot q$; where d is distance between charges and q is the elementary charge) for $Ir[tBu]-PF_6$ and $Ir[tBu]-BAr_4^F$ assuming only contact-ion pairing.

	Distance between Ir^+ and X^-	$\mu_{Predicted}$
$Ir[tBu]-PF_6$	5.7 Å	27.4 D
$Ir[tBu]-BAr_4^F$	13.0 Å	62.4 D

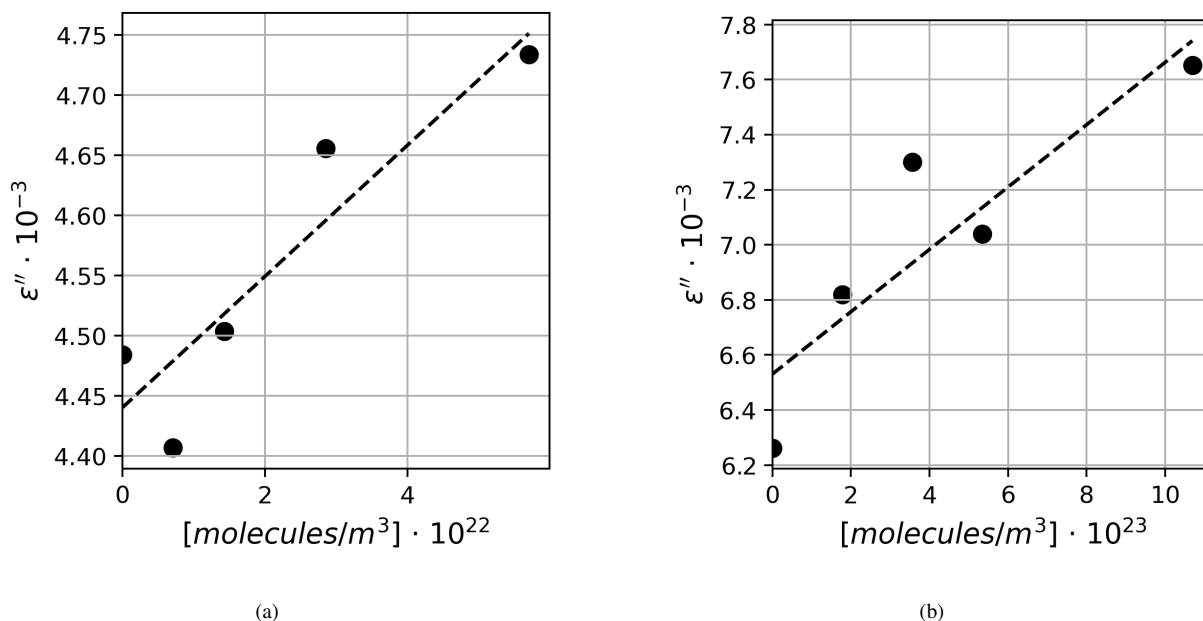


Figure 4. (a) Ground-state measurement of the imaginary permittivity as a function of $Ir[tBu]-PF_6$ concentration in 1,4-dioxane. A linear fit of the form $\epsilon'' = 5.46 \cdot 10^{-27}x + 4.44 \cdot 10^{-3}$. (b) ground-state measurement of the imaginary permittivity as a function of $Ir[tBu]-BAR_4^F$ concentration in 1,4-dioxane. A linear fit gives the form $\epsilon'' = 1.13 \cdot 10^{-27}x + 6.53 \cdot 10^{-3}$.

198 When considering the ligand framework of $Ir[tBu]^+$, a ground-state dipole moment is expected on grounds of both
 199 symmetry and formal charge distribution. However, cyclometalation of Ir(III) with $dF(CF)_3ppy$ ligands produces a highly
 200 mixed HOMO ($Ir_d-dF(CF)_3ppy$) that lies relatively close to the metal.^{12,59} This bonding environment implies that the
 201 ground-state *intramolecular* dipole in $Ir[tBu]^+$ should be relatively small. In contrast, the apparent dipole moment resulting
 202 from a contact-ion pair interaction is expected to be large, due to the relatively large separation between the ionic charge centers
 203 and the fact that the ions rotate as a single unit in solution. Directly measured dipole moments of $[Ir(C^{\wedge}N)_2(N^{\wedge}N)]^+$ complexes
 204 have never been reported to our knowledge, either in the ground or excited-states.^{10,19–21,23,31,33–36,56–58}

205 Using the slope from ϵ'' vs the concentration of $Ir[tBu]-PF_6$ in 1,4-dioxane (figure 4(a)), equation (9), and a θ_{paired} of
 206 70.5 ps (calculated assuming contact-ion pairing as described in the *Molecular Rotation* section of the SI) we found the
 207 ground-state dipole moment of $Ir[tBu]-PF_6$ to be 10.7 D. If we assume loose or no ion pairing, the rotation time is modified to
 208 68.26 ps and the calculated dipole moment is reduced to 10.6 D, only a small change occasioned by the very compact size
 209 of PF_6^- . In both cases, the magnitude of the ground-state dipole is substantially larger than what we would expect for the
 210 *intramolecular* ground-state dipole moment of just $Ir[tBu]^+$ (~ 5.0 D, based on that of $Ir(ppy)_3$ (see SI section *Non-ionic*
 211 *Iridium(III) Complex*)). Yet, the calculated value is still smaller than we expect for a contact-ion pair $Ir[tBu]-PF_6$ (27.4 D). We
 212 posit three primary explanations: first, that the inter- and intra- molecular dipoles partially cancel in a contact-ion pair that
 213 self-organizes to minimize electrostatic energy, as depicted in Figure 5a. Second, that the small PF_6^- anion may lie ~ 2.5 Å
 214 closer to the positive charge center than expected (27.4-5.0 = 22.4 D, integer charge separation produces a dipole moment of
 215 4.8 D/Å), interdigitating with the ligand shell. Third, that contact ion pair is likely to be in equilibrium with solvent-separated
 216 pairs, which would reduce the average dipole moment that we measure.

217 An excellent test of these ideas is comparison with results for the more weakly pairing anion BAR_4^F . Using the slope from
 218 ϵ'' vs. the concentration of $Ir[tBu]-BAR_4^F$ (figure 4(b)), equation (9), and a $\theta_{unpaired}$ of 68.3 ps (calculated assuming loose ion
 219 pair association); we found the ground-state dipole moments of $Ir[tBu]-BAR_4^F$ to be 4.82 D, consistent with our expectations for
 220 the range of possible dipole moment of $Ir[tBu]^+$. If we assume contact-ion pairing on the other hand, we obtain a much larger
 221 dipolar relaxation time of $\theta_{paired} = 367$ ps due to the large size of the BAR_4^F anion. Using this value we calculate a dipole
 222 moment of 10.8 D, which in this case is *far* too small to be consistent with the large *intermolecular* dipole moment expected for
 223 a contact-ion pair of $Ir[tBu]-BAR_4^F$, even when the anti-parallel vector sum of the *intramolecular* and *intermolecular* dipole
 224 moments and similar charge displacements are considered. This, combined with the consistency of the *unpaired* dipole we
 225 measure here with that of $Ir(ppy)_3$ (see Supplementary Fig. S11), leads us to conclude that contact-ion pairs are absent for

226 $Ir[tBu]-BAR_4^F$. Thus, our data is consistent with the idea that a majority of $Ir[tBu]-PF_6$ species in 1,4-dioxane form contact-ion
 227 pairs that self-organize to minimize the overall dipole moment, while the majority of $Ir[tBu]-BAR_4^F$ species exist as either
 228 solvent-separated ion pairs or dissociated ions, even in 1,4-dioxane.

229 These assignments are supported by subtle differences in absorbance and steady-state emission spectra we observe
 230 for $Ir[tBu]-PF_6$ vs $Ir[tBu]-BAR_4^F$ (See SI sections: *Absorption and emission spectroscopy* and *[Ir(C^N)₂(N^N)]X Electronic*
 231 *Structure*). The dipole moment values we obtain are also broadly consistent with prior solvatochromism measurements for
 232 $[Ir(C^N)_2(N^N)]Cl$ complexes where (C^N)= ppy or benzo[h]quinoline (bzq), and (N^N)= bpy or 1,10-phenanthroline (bpy)).⁵⁶
 233 In this study, the ground and excited-state dipole moments were determined from absorption and emission solvatochromism
 234 data in 17 solvents spanning the polarity spectrum, but neglecting to account for ion pairing behavior. Thus, in low dielectric
 235 solvents, the dipole moment they observed should be characteristic of the ion-paired species $[Ir(C^N)_2(N^N)]Cl$, whilst in
 236 high dielectric solvents it most likely represents that of the unpaired species. We conjecture that their measured value ($\mu_{Lit}=6.7$
 237 D), represents an average of these two extremes, and compares favorably with an average of the dipole moments we find for
 238 $Ir[tBu]-PF_6$ and $Ir[tBu]-BAR_4^F$ ($\mu_{Avg}=7.7$ D).

239 Figure 5 illustrates the ion-pairing behavior we propose for the ground-state without contact-ion pairing (5(a)) and with
 240 contact-ion pairing (5(b)). If the ion pair is not in contact, the overall dipole moment measured using dielectric-loss will be
 241 equal to just the *intramolecular* dipole moment (purple). However, in the presence of contact-ion pairing, the overall dipole
 242 moment measured using dielectric-loss will be equal to the vector sum (equation (14)) of the *intramolecular* dipole moment
 243 (purple) and the *intermolecular* dipole moment (yellow). Dielectric-loss can only measure ion pairs that are bound sufficiently
 244 tightly for the pair to tumble as a single molecular unit in solution. In any situation where each complex can tumble separately
 245 the measured dipole moment will revert to the *intramolecular* component depicted in Fig. 5(a), even if the ions remain paired in
 246 a looser solvent-separated fashion.²³

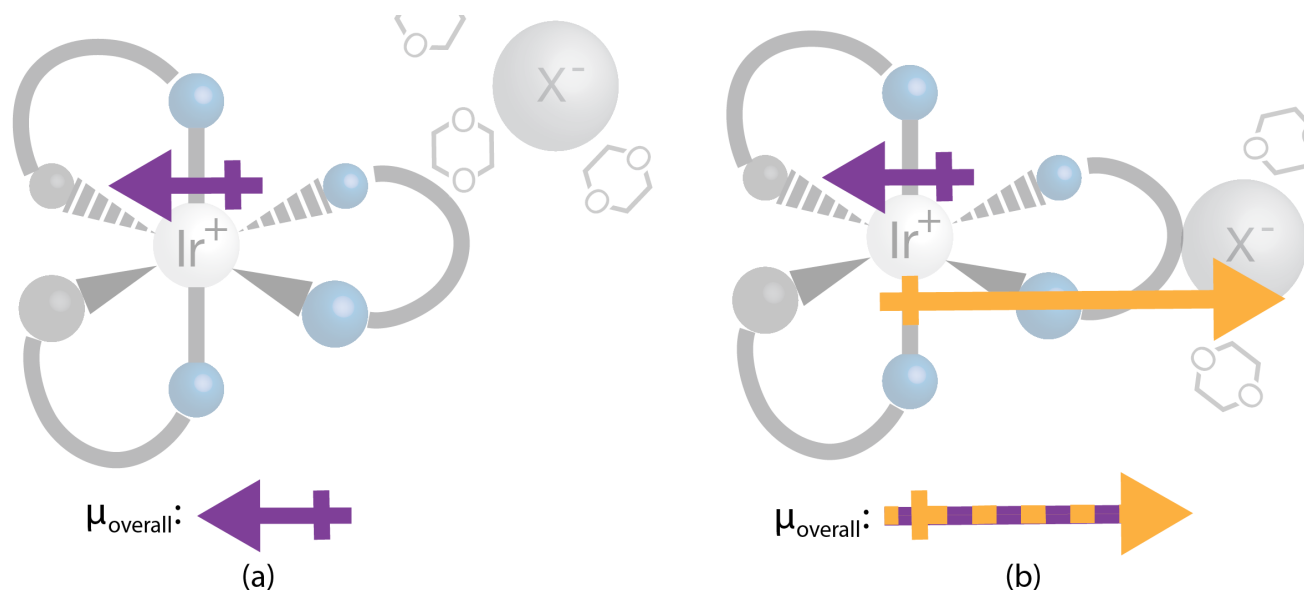


Figure 5. Overall dipole moment showing the *intramolecular* dipole (purple) and the *intermolecular* dipole (yellow). (a) Ground-state dipole configuration for a complex without contact-ion pairing, as predicted in the case of $Ir[tBu]-BAR_4^F$, showing that the signal observed using dielectric-loss will be the same as the *intramolecular* dipole moment of $Ir[tBu]^+$. (b) Ground-state dipole configuration for a contact-ion paired complex, as predicted in the case of $Ir[tBu]-PF_6$, showing the overall dipole moment observed by dielectric-loss is the vector sum (dashed arrow) of the *intramolecular* dipole moment of $Ir[tBu]^+$ and the *intermolecular* dipole moment between $Ir[tBu]^+$ and X^- .

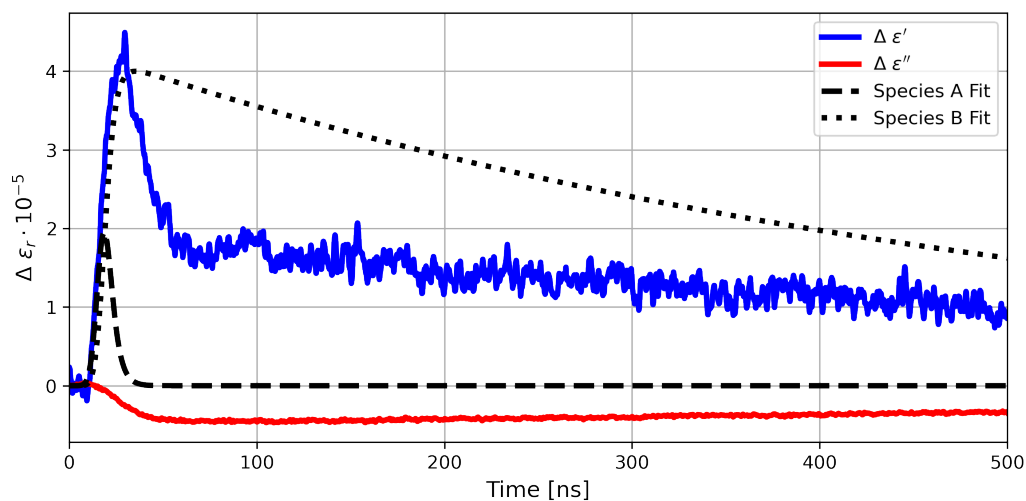
$$\mu_{overall} = |\vec{\mu}_{intra} + \vec{\mu}_{inter}| \quad (14)$$

Table 3. Ground-state dipole moments for $Ir[tBu]-PF_6$ and $Ir[tBu]-BAr_4^F$ assuming (a) separation-ion pairing and (b) contact-ion pairing.

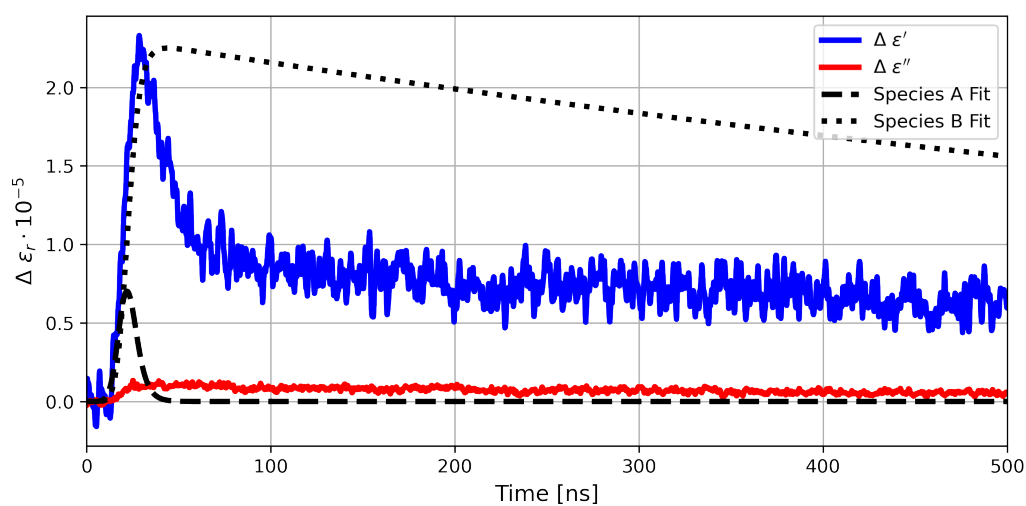
	$\epsilon''/\text{molecule}$	θ^a	μ_{GS}^a	θ^b	μ_{GS}^b
$Ir[tBu]-PF_6$	$5.45i \cdot 10^{-27}$	68.3 ps	10.6 ± 2.7 D	70.5 ps	10.7 ± 2.7 D
$Ir[tBu]-BAr_4^F$	$1.13i \cdot 10^{-27}$	68.3 ps	4.8 ± 1.4 D	367 ps	10.8 ± 3.2 D

247 Transient Dipole Moment

248 fp-TRDL was performed on both complexes to study how their dipole moments change after photoexcitation. Having
 249 observed dominant contact ion pairing in the ground-state of $Ir[tBu]-PF_6$ and minimal contact ion pairing in $Ir[tBu]-BAr_4^F$, we
 250 expect to see similar changes in their measured excited-state dipole moments. Transient data for both complexes are shown in
 251 Fig. 6 (a) ($X^- = PF_6^-$) and (b) ($X^- = BAr_4^F$). The data obtained were collected and separated into their complex permittivity
 252 components as detailed in the *Fitting COMSOL Models to Data and the Complex K-Factor* section of the SI. Both complex's
 253 kinetics were fit with a global two-Species sequential kinetic model similar to that used for DMABN. Here, however, there is
 254 less of a clear *a-priori* basis for assigning the identity of these kinetically identified Species from TRDL measurements. We
 255 simply designate the fast, early-time component as Species A and the slower, later-time component as Species B for now. The
 256 rate constants from the kinetic fits and the absolute dipole moments are summarized in table 4.



(a)



(b)

Figure 6. fp-TRDL to studies of the excited-state kinetics separating the transients into real (blue) and imaginary (red) permittivities with the kinetic fits corresponding to the early-time Species A and later-time Species B. (a) fp-TRDL transient for $Ir[tBu]-PF_6$ at a concentration of 0.23 mM, 410 nm excitation at $\sim 4.71 \cdot 10^{16} \text{ cm}^{-2}$, 7 ns FWHM pulse. The negative change in the imaginary permittivity is a result of ion pairing. (b) fp-TRDL transient for $Ir[tBu]-BAR_4^F$ at a concentration of 0.36 mM, 410 nm excitation at $\sim 1.06 \cdot 10^{16} \text{ cm}^{-2}$, 7 ns FWHM pulse. The positive change in imaginary permittivity arises from measuring the *intramolecular* dipole moment without the influence of a contact-counter ion.

Table 4. Summary of $Ir[tBu]-PF_6$ and $Ir[tBu]-BAR_4^F$ parameters from experimental data.

	State	$\epsilon_r/molecule$ (10^{-27})	μ (D)	ΔV_p (\AA^3)	Rate constant (s^{-1})
$Ir[tBu]-PF_6$	GS	5.46i	10.7 ± 2.7	–	–
	A	$\Delta(21.7 - 0.189i)$	10.9 ± 2.7	858	$2.78 \cdot 10^8$
	B	$\Delta(1.81 + 0.535i)$	10.2 ± 2.6	77.4	$1.38 \cdot 10^6$
$Ir[tBu]-BAR_4^F$	GS	1.13i	4.8 ± 1.4	–	–
	A	$\Delta(21.3 - 0.886i)$	6.4 ± 1.9	833	$2.78 \cdot 10^8$
	B	$\Delta(1.64 - 0.158i)$	5.2 ± 1.6	63.5	$8.90 \cdot 10^5$

257 While TRDL measurements can't directly report on the identity of Species A and B, the obtained time constants and
258 dipole measurements are interpreted with respect to the literature on similar Ir(III) species to help elucidate the photoexcitation
259 mechanism. Species A for both $Ir[tBu]-PF_6$ and $Ir[tBu]-BAR_4^F$ displays nearly instrument-response limited kinetics and is
260 associated with a large increase in $\Delta\epsilon'$ which is a function of the polarizability volume and the dipole moment. Since this feature
261 of Species A is present in both complexes, it is most likely a property of $Ir[tBu]^+$, and not influenced by differences in ion
262 pairing behavior. Moreover, the change in $\Delta\epsilon''$ is much smaller than $\Delta\epsilon'$, indicating that the major contribution to $\Delta\epsilon'$ is a change
263 in the polarizability volume. Two mechanisms can contribute to a change in polarizability volume; the electron cloud increasing
264 in volume, or a resonance structure where a dipole moment flips between resonances much faster than the frequency of the
265 microwave electric field (<100 ps period). Since the $dF(CF_3)ppy$ -based LUMO+1 and $dtbpy$ -based LUMO are energetically
266 similar in $Ir[tBu]^+$ (See SI, $[Ir(C^{\wedge}N)_2(N^{\wedge}N)]X$ Electronic Structure), we conclude that the change in polarizability volume
267 is due to ligand-ligand charge transfer (LLCT) dynamics described by the dipole moment shifting between the $dF(CF_3)ppy$
268 and $dtbpy$ ligand in the excited-state. This interpretation of the large $\Delta\epsilon'$ signal is consistent with previous reports on similar
269 complexes indicating that large changes in dipole upon photoexcitation result from substantial geometric distortion in the
270 $MLCT_{bpy}$ excited-states due to LLCT.^{19, 20, 56, 58, 60, 61} Moreover, we observe at least two emissive bands in the emission profile
271 of both $Ir[tBu]-PF_6$ and $Ir[tBu]-BAR_4^F$ (See SI, Absorbance and emission spectroscopy). The origin of multiple emission bands
272 in $[Ir(ppy)_2(bpy)]PF_6$ is elucidated in previous work, and the photoinitiated excited-state dynamics are described as follows:
273 (1) the Franck-Condon excited-states form in <30 ps then decay to (2) a 3LLCT state formed within 2.6 ns, (3) a ${}^3MLCT_{ppy}$
274 formed in <0.4 ns, and (4) a ${}^3MLCT_{bpy}$ formed within 4.8 ns (all time constants are from toluene measurements).⁵⁸ This
275 previous work describes emission from the 3LLCT , ${}^3MLCT_{ppy}$, and ${}^3MLCT_{bpy}$ in τ_{em} = 617, 643, and 582 ns, respectively in
276 toluene, with the intensity of each band depending on the relative population of each state (see Fig. 7).

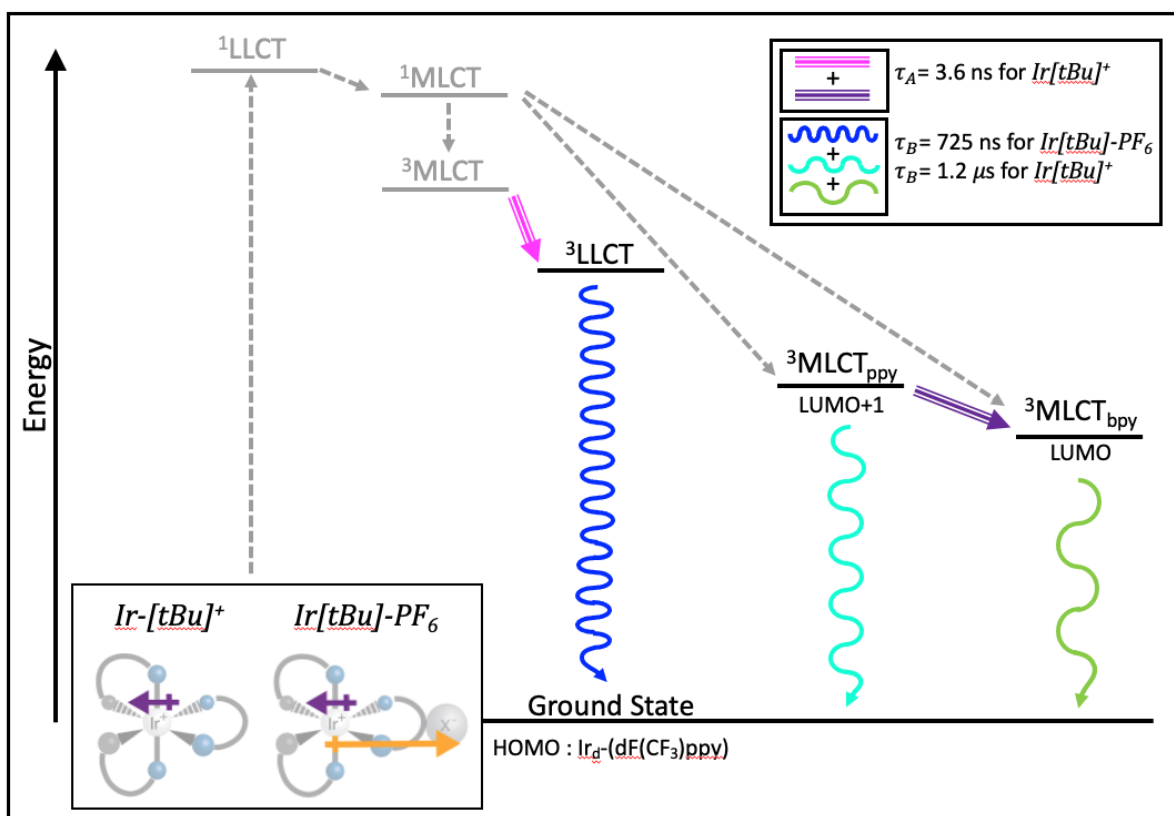


Figure 7. The proposed excited-state dynamics of $Ir[tBu]-PF_6$ and $Ir[tBu]-BAR_4^F$ (i.e. the unpaired $Ir[tBu]^+$ ion) in 1,4-dioxane based on the TRDL transients, and absorption and emission spectra ($\lambda_{ex} = 415$ nm). The transitions that occur within our system's IRF are included in grey and lead to Species A where the dipole moment of both Species is greater than its ground-state value. As Species A (${}^1LLCT + {}^1MLCT + {}^3MLCT + {}^3MLCT_{ppy}$) decays to the emissive states of Species B (${}^3LLCT + {}^3MLCT_{ppy} + {}^3MLCT_{bpy}$), the PF_6^- counterion moves to cancel the intramolecular dipole. This rearrangement results in a dipole moment in Species B that is smaller than that of the ground-state for $Ir[tBu]-PF_6$ and stabilization of the emitting state energies. In contrast, the Species B dipole in $Ir[tBu]-BAR_4^F$ is larger than its ground-state value, representing the dipole dynamics of unpaired $Ir[tBu]^+$.

277 Considering the instrument response function of our system and the differing dielectric constants of toluene vs 1,4-dioxane,
 278 the literature mechanism described above agrees well with the measured time constant associated Species A's decay ($2.78 \cdot 10^8$
 279 s^{-1} , i.e. $\tau_A = 3.60$ ns), which likely represents a rough average of the time constants associated with processes (2) and (4)
 280 above ($\tau_{avg} = 3.70$ ns). The literature τ_{em} values also agree well with our time-integrated decay constant of Species B in
 281 $Ir[tBu]-PF_6$, $\tau_B = 725$ ns (see table 4), considering their work was performed on $[Ir(ppy)_2(bpy)]PF_6$ and the reported time
 282 constants varied with solvent dielectric environment. Notably, Wu et al., estimates the excited-state dipole to be ~ 6.4 D based
 283 on solvent induced shifting of the high energy emission band (470 nm in toluene, 23°C) using the Mataga-Lippert equation.
 284 As this emission band is attributed to the 3LLCT and does not account for ion-pairing, this is in excellent agreement with our
 285 calculation for Species A of $Ir[tBu]-BAR_4^F$.

286 Immediately after excitation, $\Delta\epsilon''$ is similar in both complexes during the evolution of Species A. The dipole moment of
 287 Species A increases in both complexes relative to their respective ground-states, and this accompanies the formation of the
 288 Frank-Condon excited-states discussed above (large polarizability volume) seen in the $\Delta\epsilon'$ transient. However, as the system
 289 evolves to Species B, $Ir[tBu]-PF_6$ exhibits a *negative* change in the dipole moment (relative to the ground-state) whereas
 290 $Ir[tBu]-BAR_4^F$ continues to exhibit a continued positive change.

291 In both $Ir[tBu]-PF_6$ and $Ir[tBu]-BAR_4^F$, Species B's kinetics align with those reported for its emissive states (and our measured
 292 photoluminescence for $Ir[tBu]-PF_6$, see Supplementary Fig. S8 and S9), and $\Delta\epsilon'$ and $\Delta\epsilon''$ evolve together. As mentioned in the
 293 literature on $[Ir(ppy)_2(bpy)]^+$, the emissive states have such similar lifetimes that they are difficult to differentiate.^{58,60,61} The
 294 negative $\Delta\epsilon''$ from $Ir[tBu]-PF_6$ indicates that the observed excited-state dipole moment associated with the relaxed MLCT state
 295 is less than that of its ground-state. This striking observation is consistent with a sub-nanosecond excited-state reorganization

296 mechanism where the ion pair reorients to cancel the *intramolecular* dipole moment of the MLCT state, as inferred for the
 297 ground-state in the preceding section. Indeed, contact-ion pairing combined with this sort of excited-state reorganization will
 298 *always* result in an overall negative change in the dipole moment. Simply by virtue of the fact that the counter-ion must remain
 299 further from the molecular center than the ligand shell, it is impossible for the *intramolecular* dipole moment to exceed that
 300 associated with the *intermolecular* dipole moment. The fact that we do not see this negative change in the B Species of the
 301 $Ir[tBu]-BAR_4^F$ complex is confirmation that the negative transient dipole moment is most likely due to ion-pair reorganization.
 302 As described previously on similar complexes, ion-pairing imposes an electrostatic restriction on the spatial geometry of the
 303 complex.^{35,36} This description agrees well with the differences we observe in the ground-state dipole moments and absorption
 304 spectra of $Ir[tBu]-BAR_4^F$ vs $Ir[tBu]-PF_6$ (See SI, *Absorbance and emission spectroscopy*). However, the ion-pair rearrangement
 305 in the excited-state alters the geometry of the coordination sphere to accommodate the charge redistribution. This rearrangement
 306 results in a slight stabilization of the emitting states. This stabilizing effect is evidenced by small bathochromic shifts in the
 307 emission bands, differences in the population of the ${}^3MLCT_{dF(CF_3)ppy/dtbpy}$ (See Supplementary Fig. S8 and Supplementary
 308 Table S7), and a reduction of the excited-state lifetime. The observed shifts in emission profile and reduction in the lifetime for
 309 $Ir[tBu]-PF_6$ vs $Ir[tBu]-BAR_4^F$ also agree well with previous literature results.^{19,32,33,35,36}

310 In both complexes, $\Delta\epsilon'$ shows a much larger charge delocalization for Species A over Species B, as inferred from the large
 311 polarizability volume.⁶² This makes sense in light of the highly mixed nature of the Frank-Condon and high-lying excited-states
 312 that result in LLCT. This could be important to understanding and improving the efficiency of a photoredox catalyst since the
 313 charges in Species A are more dispersed than in Species B. Extending the lifetime of Species A or chemically pre-associating
 314 the photoredox catalyst with target substrate could enhance the likelihood of charge transfer due to Species A having a larger
 315 dispersion of charge and thus improve the overall reaction.

316 Data from the $Ir[tBu]-BAR_4^F$ complex provides the magnitude of the *intramolecular* dipole moment, which we use to
 317 compute absolute dipoles for each excited-state Species in table 4. We find that the dipole moment we observe for $Ir[tBu]-BAR_4^F$
 318 does not meet with our simplistic center-of-mass approximation, which suggests an MLCT-state dipole moment of 16.8 D.
 319 Instead, we observe a transient dipole moment of only 5.2 ± 1.6 D in the fully relaxed MLCT (Species B). This discrepancy
 320 could partly be accounted for if the ground and excited-state dipole moments oppose each other. However, even exact opposition
 321 would not make up the whole difference. We can eliminate the possibility that the small observed transient dipole moment is
 322 a more subtle manifestation of ion-pair reorganization by BAR_4^F , as the neutral homoleptic complex $Ir(ppy)_3$ (see SI section
 323 *Non-ionic Iridium(III) Complex*) displays an even smaller change in excited-state dipole moment (see Supplementary Table S6).
 324 Rather, we posit that the excited-state dipole moment is intrinsically small in these complexes, consistent with the high degree
 325 of mixing between the orbitals involved. This indicates that the simplistic picture of the lowest MLCT state as an integer charge
 326 localized on the bpy ligand is incorrect for this complex, and is likely similar in other related Ir(III) photoredox catalysts.

327 Knowing the *intramolecular* dipole moment and the observed dipole moment of the $Ir[tBu]-PF_6$ complex, the approximate
 328 distance between the iridium cation and phosphorous anion can be calculated using equation (14) for the ground-state and each
 329 excited-state Species. Table 5 summarizes this change in distance for $Ir[tBu]-PF_6$.

Table 5. Approximate distances between the iridium cation and phosphorus anion for each state.

	Ground-state	Species A	Species B
Distance (Å)	4.2 ± 2	4.3 ± 2	3.9 ± 2

330 Distance calculations show that the PF_6^- counter anion is not effected by Species A, this could be because the ground-state
 331 dipole of the $Ir[tBu]^+$ is pointing in the same direction as the Species A dipole, or because Species A decays faster than the
 332 reorganizational response time of the PF_6^- counter anion. In Species B, the distance between the ions decrease by 0.4 Å which
 333 can be explained by the *intramolecular* dipole moment of $Ir[tBu]^+$ reorganizing to point away from the $dF(CF_3)ppy$ ligands
 334 as the excited electron settles closer to the dtbpy ligand. This change in dipole direction causes the PF_6^- counter anion to
 335 move between the two $dF(CF_3)ppy$ ligands of the $Ir[tBu]^+$ complex which, due to the smaller size of the $dF(CF_3)ppy$ ligands
 336 compared to the *dtbpy* ligand, allows the PF_6^- to get closer to the positively-charged iridium center.

337 Conclusion

338 In this work we have applied modern computational methods to revitalize time-resolved dielectric-loss spectroscopy as a
 339 foundational tool for studying the ground and excited-state electronic configuration of molecules in solution. Electromagnetic
 340 simulations of the microwave cavity response function and calculation of molecular dipolar relaxation time improve on the
 341 accuracy and broad applicability of the technique. We verify our methods by showing agreement with past literature on the
 342 model compound N,N-dimethylaminobenzonitrile. Application of TRDL to ($[Ir[dF(CF_3)ppy]_2(dtbbpy)]X$), a photocatalyst of
 343 great interest in the modern renaissance of light escalated chemistry, reveals dramatic changes in the dipole moment in both

344 ground and excited-states depending on the identity of the counterion X^- . Contact-ion pairing is observed in 1,4-dioxane
345 when $X = PF_6^-$, and there is a *negative* change in the dipole moment upon photoexcitation. In contrast, when $X = BA_r_4^F$
346 we observe no evidence of contact ion pairs, and the change in dipole moment upon photoexcitation is *positive*, as expected.
347 These results are consistent with an excited-state ion-pair reorganization mechanism that cancels the dipole moment of the
348 lowest-lying MLCT state when $X = PF_6^-$. We suggest that this phenomenon may explain the recently observed dependence
349 of photocatalytic activity on counter-ion identity in similar iridium(III)-based photocatalysts. Ion pair reorganisation can be
350 expected to reduce the excited-state potential energy and the proposed migration of the counter anion to the most positively
351 charged region of the complex may limit the ability of these catalysts to drive oxidative chemistry. Finally, unrelated to ion pair
352 dynamics, the measured dipole moment of the relaxed $MLCT_{dtbpy}$ state in $[Ir[dF(CF_3)ppy]_2(dtbpy)]X$ is much smaller than
353 naive point-charge calculations suggest, which, combined with a small polarizability volume indicate a rather localized final
354 state of mixed metal-ligand character, in contrast with the highly polarizable initial $MLCT$ states observed on the timescale
355 of our instrument response. Future work should explicitly test to what extent ion pair reorganisation, the excited-state dipole
356 moment and polarizability volume of photoredox catalysts may influence their reactivity.

357 References

- 358 1. Wagenknecht, P. S. & Ford, P. C. Metal centered ligand field excited states: Their roles in the design and performance of
359 transition metal based photochemical molecular devices. *Coord. Chem. Rev.* **255**, 591–616, DOI: [10.1016/j.ccr.2010.11.016](https://doi.org/10.1016/j.ccr.2010.11.016)
360 (2011).
- 361 2. Sakai, H. A., Liu, W., Le, C. & MacMillan, D. W. Cross-Electrophile Coupling of Unactivated Alkyl Chlorides. *J. Am.*
362 *Chem. Soc.* **142**, 11691–11697, DOI: [10.1021/jacs.0c04812](https://doi.org/10.1021/jacs.0c04812) (2020).
- 363 3. Chen, T. Q. & MacMillan, D. W. A Metallaphotoredox Strategy for the Cross-Electrophile Coupling of α -Chloro Carbonyls
364 with Aryl Halides. *Angewandte Chemie - Int. Ed.* **58**, 14584–14588, DOI: [10.1002/anie.201909072](https://doi.org/10.1002/anie.201909072) (2019).
- 365 4. Nguyen, S. T., Murray, P. R. & Knowles, R. R. Light-driven depolymerization of native lignin enabled by proton-coupled
366 electron transfer. *ACS Catal.* **10**, 800–805, DOI: [10.1021/acscatal.9b04813](https://doi.org/10.1021/acscatal.9b04813) (2020).
- 367 5. Zhang, J. Conversion of Lignin Models by Photoredox Catalysis. *ChemSusChem* **11**, 3071–3080, DOI: [10.1002/cssc.](https://doi.org/10.1002/cssc.201801370)
368 [201801370](https://doi.org/10.1002/cssc.201801370) (2018).
- 369 6. Daub, M. E. *et al.* Enantioselective [2+2] Cycloadditions of Cinnamate Esters: Generalizing Lewis Acid Catalysis of
370 Triplet Energy Transfer. *J. Am. Chem. Soc.* **141**, 9543–9547, DOI: [10.1021/jacs.9b04643](https://doi.org/10.1021/jacs.9b04643) (2019).
- 371 7. Zhou, Y., Xiong, Z., Qiu, J., Kong, L. & Zhu, G. Visible light photocatalytic acyldifluoroalkylation of unactivated alkenes
372 for the direct synthesis of: Gem -difluorinated ketones. *Org. Chem. Front.* **6**, 1022–1026, DOI: [10.1039/c9qo00136k](https://doi.org/10.1039/c9qo00136k)
373 (2019).
- 374 8. Arias-Rotondo, D. M. & McCusker, J. K. The photophysics of photoredox catalysis: A roadmap for catalyst design. *Chem.*
375 *Soc. Rev.* **45**, 5803–5820, DOI: [10.1039/c6cs00526h](https://doi.org/10.1039/c6cs00526h) (2016).
- 376 9. Porras, J. A., Mills, I. N., Transue, W. J. & Bernhard, S. Highly Fluorinated Ir(III)-2,2':6',2''-Terpyridine-Phenylpyridine-X
377 Complexes via Selective C-F Activation: Robust Photocatalysts for Solar Fuel Generation and Photoredox Catalysis. *J.*
378 *Am. Chem. Soc.* **138**, 9460–9472, DOI: [10.1021/jacs.6b03246](https://doi.org/10.1021/jacs.6b03246) (2016).
- 379 10. You, N., Kim, K. S., Ahn, T. K., Kim, D. & Park, S. Y. Direct spectroscopic observation of interligand energy transfer in
380 cyclometalated heteroleptic iridium(III) complexes: A strategy for phosphorescence color tuning and white light generation.
381 *J. Phys. Chem. C* **111**, 4052–4060, DOI: [10.1021/jp0702550](https://doi.org/10.1021/jp0702550) (2007).
- 382 11. Lowry, M. S. *et al.* Single-layer electroluminescent devices and photoinduced hydrogen production from an ionic
383 iridium(III) complex. *Chem. Mater.* **17**, 5712–5719, DOI: [10.1021/cm051312+](https://doi.org/10.1021/cm051312+) (2005).
- 384 12. De Angelis, F. *et al.* Controlling phosphorescence color and quantum yields in cationic iridium complexes: A combined
385 experimental and theoretical study. *Inorg. Chem.* **46**, 5989–6001, DOI: [10.1021/ic700435c](https://doi.org/10.1021/ic700435c) (2007).
- 386 13. Radwan, Y. K., Maity, A. & Teets, T. S. Manipulating the Excited States of Cyclometalated Iridium Complexes with
387 β -Ketoiminate and β -Diketiminato Ligands. *Inorg. Chem.* **54**, 7122–7131, DOI: [10.1021/acs.inorgchem.5b01401](https://doi.org/10.1021/acs.inorgchem.5b01401) (2015).
- 388 14. Spaenig, F. *et al.* Excited-state properties of heteroleptic iridium(III) complexes bearing aromatic hydrocarbons with
389 extended cores. *Inorg. Chem.* **50**, 10859–10871, DOI: [10.1021/ic201397v](https://doi.org/10.1021/ic201397v) (2011).
- 390 15. Lowry, M. S. & Bernhard, S. Synthetically tailored excited states: Phosphorescent, cyclometalated iridium(III) complexes
391 and their applications. *Chem. - A Eur. J.* **12**, 7970–7977, DOI: [10.1002/chem.200600618](https://doi.org/10.1002/chem.200600618) (2006).

- 392 **16.** Slinker, J. D. *et al.* Efficient Yellow Electroluminescence from a Single Layer of a Cyclometalated Iridium Complex. *J.*
393 *Am. Chem. Soc.* **126**, 2763–2767, DOI: [10.1021/ja0345221](https://doi.org/10.1021/ja0345221) (2004).
- 394 **17.** Lowry, M. S., Hudson, W. R., Pascal, R. A. & Bernhard, S. Accelerated luminophore discovery through combinatorial
395 synthesis. *J. Am. Chem. Soc.* **126**, 14129–14135, DOI: [10.1021/ja047156+](https://doi.org/10.1021/ja047156+) (2004).
- 396 **18.** Diluzio, S. *et al.* High-Throughput Screening and Automated Data-Driven Analysis of the Triplet Photophysical Properties
397 of Structurally Diverse, Heteroleptic Iridium(III) Complexes. *J. Am. Chem. Soc.* **143**, 1179–1194, DOI: [10.1021/jacs.](https://doi.org/10.1021/jacs.0c12290)
398 [0c12290](https://doi.org/10.1021/jacs.0c12290) (2021).
- 399 **19.** Tschierlei, S. *et al.* Ultrafast excited state dynamics of iridium(III) complexes and their changes upon immobilisation onto
400 titanium dioxide layers. *Phys. Chem. Chem. Phys.* **18**, 10682–10687, DOI: [10.1039/c6cp00343e](https://doi.org/10.1039/c6cp00343e) (2016).
- 401 **20.** Li, J. *et al.* Synthetic Control of Excited-State Properties in Cyclometalated Ir(III) Complexes Using Ancillary Ligands.
402 *Inorg. Chem.* **44**, 1713–1727, DOI: [10.1021/ic048599h](https://doi.org/10.1021/ic048599h) (2005).
- 403 **21.** Balzani, V., Sabbatini, N. & Scandola, F. “Second-Sphere” Photochemistry and Photophysics of Coordination Compounds.
404 *Chem. Rev.* **86**, 319–337, DOI: [10.1021/cr00072a002](https://doi.org/10.1021/cr00072a002) (1986).
- 405 **22.** Marcus, Y. & Hefter, G. Ion pairing. *Chem. Rev.* **106**, 4585–4621, DOI: [10.1021/cr040087x](https://doi.org/10.1021/cr040087x) (2006).
- 406 **23.** Macchioni, A. Ion pairing in transition-metal organometallic chemistry. *Chem. Rev.* **105**, 2039–2073, DOI: [10.1021/](https://doi.org/10.1021/cr0300439)
407 [cr0300439](https://doi.org/10.1021/cr0300439) (2005).
- 408 **24.** Tsuboi, T. Optical and Thermal Electron Transfer in KCl: Tl+ Crystals. *Zeitschrift fur Naturforschung - Sect. A J. Phys.*
409 *Sci.* **33**, 1154–1157, DOI: [10.1515/zna-1978-1005](https://doi.org/10.1515/zna-1978-1005) (1978).
- 410 **25.** Farney, E. P. *et al.* Discovery and Elucidation of Counteranion Dependence in Photoredox Catalysis. *J. Am. Chem. Soc.*
411 **141**, 6385–6391, DOI: [10.1021/jacs.9b01885](https://doi.org/10.1021/jacs.9b01885) (2019).
- 412 **26.** Strauss, S. H. The Search for Larger and More Weakly Coordinating Anions. *Chem. Rev.* **93**, 927–942, DOI: [10.1021/](https://doi.org/10.1021/cr00019a005)
413 [cr00019a005](https://doi.org/10.1021/cr00019a005) (1993).
- 414 **27.** Appelhans, L. N. *et al.* An anion-dependent switch in selectivity results from a change of C-H activation mechanism in the
415 reaction of an imidazolium salt with IrH 5(PPh3)2. *J. Am. Chem. Soc.* **127**, 16299–16311, DOI: [10.1021/ja055317j](https://doi.org/10.1021/ja055317j) (2005).
- 416 **28.** Song, L. & Trogler, W. C. Mechanism of Halide-Induced Disproportionation of M(CO)3(PCy3)2+ 17-Electron Radicals
417 (M = Fe, Ru, Os). Periodic Trends on Reactivity and the Role of Ion Pairs *Lin. Tech. Rep.* (1992).
- 418 **29.** Troian-Gautier, L., Beauvilliers, E. E., Swords, W. B. & Meyer, G. J. Redox Active Ion-Paired Excited States Undergo
419 Dynamic Electron Transfer. *J. Am. Chem. Soc.* **138**, 16815–16826, DOI: [10.1021/jacs.6b11337](https://doi.org/10.1021/jacs.6b11337) (2016).
- 420 **30.** Uraguchi, D., Kimura, Y., Ueoka, F. & Ooi, T. Urea as a Redox-Active Directing Group under Asymmetric Photocatalysis
421 of Iridium-Chiral Borate Ion Pairs. *J. Am. Chem. Soc.* **142**, 19462–19467, DOI: [10.1021/jacs.0c09468](https://doi.org/10.1021/jacs.0c09468) (2020).
- 422 **31.** Tellers, D. M., Yung, C. M., Arndtsen, B. A., Adamson, D. R. & Bergman, R. G. Electronic and medium effects on the rate
423 of arene C-H bond activation by cationic Ir(III) complexes. *J. Am. Chem. Soc.* **124**, 1400–1410, DOI: [10.1021/ja011809u](https://doi.org/10.1021/ja011809u)
424 (2002).
- 425 **32.** Morton, C. M. *et al.* C-H Alkylation via Multisite-Proton-Coupled Electron Transfer of an Aliphatic C-H Bond. DOI:
426 [10.1021/jacs.9b06834](https://doi.org/10.1021/jacs.9b06834) (2019).
- 427 **33.** Ruccolo, S., Qin, Y., Schnedermann, C. & Nocera, D. G. General Strategy for Improving the Quantum Efficiency of
428 Photoredox Hydroamidation Catalysis. *J. Am. Chem. Soc.* **140**, 14926–14937, DOI: [10.1021/jacs.8b09109](https://doi.org/10.1021/jacs.8b09109) (2018).
- 429 **34.** Marton, A. *et al.* Static and dynamic quenching of Ru(II) polypyridyl excited states by iodide. *Inorg. Chem.* **45**, 362–369,
430 DOI: [10.1021/ic051467j](https://doi.org/10.1021/ic051467j) (2006).
- 431 **35.** Vining, W. J., Caspar, J. V. & Meyer, T. J. The influence of environmental effects on excited-state lifetimes. The effect of
432 ion pairing on metal-to-ligand charge transfer excited states. *J. Phys. Chem.* **89**, 1095–1099, DOI: [10.1021/j100253a010](https://doi.org/10.1021/j100253a010)
433 (1985).
- 434 **36.** Ward, W. M., Farnum, B. H., Siegler, M. & Meyer, G. J. Chloride ion-pairing with Ru(II) polypyridyl compounds in
435 dichloromethane. *J. Phys. Chem. A* **117**, 8883–8894, DOI: [10.1021/jp404838z](https://doi.org/10.1021/jp404838z) (2013).
- 436 **37.** Prier, C. K., Rankic, D. A. & MacMillan, D. W. C. Visible Light Photoredox Catalysis with Transition Metal Complexes:
437 Applications in Organic Synthesis. *Chem. Rev.* **113**, 5322–5363, DOI: [10.1021/cr300503r](https://doi.org/10.1021/cr300503r) (2013).
- 438 **38.** Smith, R. T. *et al.* Metallaphotoredox-Catalyzed Cross-Electrophile C sp³–C sp³ Coupling of Aliphatic Bromides. *J. Am.*
439 *Chem. Soc.* **140**, 17433–17438, DOI: [10.1021/jacs.8b12025](https://doi.org/10.1021/jacs.8b12025) (2018).

- 440 **39.** Britz, A. *et al.* Site-Selective Real-Time Observation of Bimolecular Electron Transfer in a Photocatalytic System Using
441 L-Edge X-Ray Absorption Spectroscopy**. *ChemPhysChem* **22**, 693–700, DOI: [10.1002/cphc.202000845](https://doi.org/10.1002/cphc.202000845) (2021).
- 442 **40.** Warman, J. M., Jonker, S. A., de Haas, M. P., Verhoeven, J. W. & Paddon-Row, M. N. <title>Photon-induced charge
443 separation in molecular systems studied by time-resolved microwave conductivity: molecular optoelectric switches</title>.
444 *Photopolym. Device Physics, Chem. Appl. II* **1559**, 159–170, DOI: [10.1117/12.506666](https://doi.org/10.1117/12.506666) (1991).
- 445 **41.** Fessenden, R. W. & Hitachi, A. A study of the dielectric relaxation behavior of photoinduced transient species. *J. Phys.*
446 *Chem.* **91**, 3456–3462, DOI: [10.1021/j100296a070](https://doi.org/10.1021/j100296a070) (1987).
- 447 **42.** Hoogesteger, F. J. *et al.* Photoinduced intramolecular charge separation in donor/acceptor-substituted bicyclohexylidene
448 and bicyclohexyl. *Chem. - A Eur. J.* **6**, 2948–2959, DOI: [10.1002/1521-3765\(20000818\)6:16<2948::AID-CHEM2948>3.0.CO;2-0](https://doi.org/10.1002/1521-3765(20000818)6:16<2948::AID-CHEM2948>3.0.CO;2-0) (2000).
- 450 **43.** Onimisi, M. Y., I. J. Comparative Analysis of Dielectric Constant and Loss Factor of Pure Butan-1-ol and Ethanol. *Am. J.*
451 *Condens. Matter Phys.* **5**, 69–75, DOI: [10.5923/j.ajcmp.20150503.02](https://doi.org/10.5923/j.ajcmp.20150503.02) (2015).
- 452 **44.** Fessenden, R. W., Carton, P. M., Shimamori, H. & Scalano, J. C. Measurement of the dipole moments of excited states and
453 photochemical transients by microwave dielectric absorption. *J. Phys. Chem.* **86**, 3803–3811, DOI: [10.1021/j100216a020](https://doi.org/10.1021/j100216a020)
454 (1982).
- 455 **45.** Reid, O. G. *et al.* Quantitative analysis of time-resolved microwave conductivity data. *J. Phys. D: Appl. Phys.* **50**, DOI:
456 [10.1088/1361-6463/aa9559](https://doi.org/10.1088/1361-6463/aa9559) (2017).
- 457 **46.** De Haas, M. P. & Warman, J. M. Photon-induced molecular charge separation studied by nanosecond time-resolved
458 microwave conductivity. *Chem. Phys.* **73**, 35–53, DOI: [10.1016/0301-0104\(82\)85148-3](https://doi.org/10.1016/0301-0104(82)85148-3) (1982). [0301-0104\(82\)85148-3](https://doi.org/10.1016/0301-0104(82)85148-3).
- 459 **47.** Schuddeboom, W., Warman, J. M., Van der Auweraer, M., de Schryver, F. C. & Declercq, D. D. Dipolar exciton states of
460 molecules with threefold symmetry. *Chem. Phys. Lett.* **222**, 586–591, DOI: [10.1016/0009-2614\(94\)00401-3](https://doi.org/10.1016/0009-2614(94)00401-3) (1994).
- 461 **48.** Warman, J. M., De Haas, M. P., Hummel, A., Varma, C. A. & Van Zeyl, P. H. Dipole moment changes in the singlet and
462 triplet excited states of 4-dimethylamino-4'-nitrostilbene detected by nanosecond time-resolved microwave conductivity.
463 *Chem. Phys. Lett.* **87**, 83–86, DOI: [10.1016/0009-2614\(82\)83560-4](https://doi.org/10.1016/0009-2614(82)83560-4) (1982).
- 464 **49.** Jonker, S. A. & Warman, J. M. Highly dipolar excited states of a symmetrical bound dimer of dimethylaminobenzonitrile
465 observed by TRMC. *Chem. Phys. Lett.* **185**, 36–40, DOI: [10.1016/0009-2614\(91\)80135-K](https://doi.org/10.1016/0009-2614(91)80135-K) (1991).
- 466 **50.** Ma, C. *et al.* Excited states of 4-aminobenzonitrile (ABN) and 4-dimethylaminobenzonitrile (DMABN): Time-resolved
467 resonance Raman, transient absorption, fluorescence, and ab initio calculations. *J. Phys. Chem. A* **106**, 3294–3305, DOI:
468 [10.1021/jp012765e](https://doi.org/10.1021/jp012765e) (2002).
- 469 **51.** Okada, T. *et al.* Time-resolved spectroscopy of DMABN and its cage derivatives 6-cyanobenzquinuclidine (CBQ) and
470 benzquinuclidine (BQ). *Chem. Phys.* **241**, 327–337, DOI: [10.1016/S0301-0104\(98\)00411-X](https://doi.org/10.1016/S0301-0104(98)00411-X) (1999).
- 471 **52.** Schuddeboom, W. *et al.* Excited-state dipole moments of dual fluorescent 4-(dialkylamino)benzonitriles. Influence of alkyl
472 chain length and effective solvent polarity. *J. Phys. Chem.* **96**, 10809–10819, DOI: [10.1021/j100205a041](https://doi.org/10.1021/j100205a041) (1992).
- 473 **53.** Visser, R. J., Weisenborn, P. C. M. & Varma, C. A. G. O. Dipole moments of singlet and triplet excited states of 4-N,N-
474 dimethylaminobenzonitrile and related compounds and of their solute-solvent exciplexes. **104**, DOI: [10.1021/j100205a041](https://doi.org/10.1021/j100205a041)
475 (1984).
- 476 **54.** Demeter, A. & Zachariasse, K. A. Triplet state dipole moments of aminobenzonitriles. *J. Phys. Chem. A* **112**, 1359–1362,
477 DOI: [10.1021/jp0747959](https://doi.org/10.1021/jp0747959) (2008).
- 478 **55.** You, Y. & Nam, W. Photofunctional triplet excited states of cyclometalated Ir(III) complexes: Beyond electroluminescence.
479 *Chem. Soc. Rev.* **41**, 7061–7084, DOI: [10.1039/c2cs35171d](https://doi.org/10.1039/c2cs35171d) (2012).
- 480 **56.** Wilde, A. P., King, K. A. & Watts, R. J. Resolution and analysis of the components in dual emission of mixed-chelate/ortho-
481 metalate complexes of iridium(III). *J. Phys. Chem.* **95**, 629–634, DOI: [10.1021/j100155a026](https://doi.org/10.1021/j100155a026) (1991).
- 482 **57.** Scattergood, P. A. *et al.* Unravelling the Mechanism of Excited-State Interligand Energy Transfer and the Engineering of
483 Dual Emission in [Ir(C ^ N) 2 (N ^ N)] + Complexes. **22**, 29, DOI: [10.1021/acs.inorgchem.9b03003](https://doi.org/10.1021/acs.inorgchem.9b03003) (2021).
- 484 **58.** Wu, S. H. *et al.* Dynamics of the excited states of [Ir(ppy)2bpy]+ with triple phosphorescence. *J. Phys. Chem. A* **114**,
485 10339–10344, DOI: [10.1021/jp102264q](https://doi.org/10.1021/jp102264q) (2010).
- 486 **59.** Hay, P. J. Theoretical studies of the ground and excited electronic states in cyclometalated phenylpyridine Ir(III) complexes
487 using density functional theory. *J. Phys. Chem. A* **106**, 1634–1641, DOI: [10.1021/jp013949w](https://doi.org/10.1021/jp013949w) (2002).

- 488 **60.** King, K. A. & Watts, R. J. Dual Emission from an Ortho-Metalated Ir(III) Complex. *J. Am. Chem. Soc.* **109**, 1589–1590,
489 DOI: [10.1021/ja00239a060](https://doi.org/10.1021/ja00239a060) (1987).
- 490 **61.** Wilde, A. P. & Watts, R. J. Solvent effects on metal-to-Ligand charge-transfer bands in ortho-metalated complexes of
491 iridium(III): Estimates of transition dipole moments. *J. Phys. Chem.* **95**, 622–629, DOI: [10.1021/j100155a025](https://doi.org/10.1021/j100155a025) (1991).
- 492 **62.** Piet, J. J., Warman, J. M., Baumgarten, M. & Müllen, K. Dipolar excitonic states of oligo-anthrylenes. *J. Phys. Chem. A*
493 **106**, 2318–2321, DOI: [10.1021/jp012870o](https://doi.org/10.1021/jp012870o) (2002).

494 **Acknowledgements**

495 This work was supported by the US Department of Energy, Office of Science, as part of BioLEC EFRC under grant
496 DE-SC0019370.

497
498 This work was authored, in part, by the National Renewable Energy Laboratory, operated by Alliance for Sustainable
499 Energy, LLC, for the U.S. Department of Energy (DOE) under Contract No. DE-AC36-08GO28308.

500
501 This article is submitted in fond memory of the late Professor John Warman (TU Delft, NL 1939-2020), whose seminal
502 research laid the foundation for transient microwave spectroscopy, and the dielectric loss spectroscopy that is described here.

503 **Author contributions statement**

504 G.R., O.G.R., J.D.E., A.Z., and J.K.M conceived the experiments; O.G.R., J.D.E., A.Z., and Z.J.M conducted the
505 experiments; G.R., O.G.R., J.D.E., A.Z., M.S.L., and H.H.R. analyzed the results; H.H.R. performed synthesis. All authors
506 reviewed and contributed to development of the manuscript.

Supplementary Files

This is a list of supplementary files associated with this preprint. Click to download.

- [SIDipoleMomentandChargeReorganizationinPhotoredoxCatalysts.pdf](#)